

**Coseismic Slip of the 2010 Mw 8.8 Great Maule, Chile, Earthquake  
Quantified by the Inversion of GRACE Observations**

Lei Wang<sup>1</sup>, C.K. Shum<sup>1</sup>, Frederik J. Simons<sup>2</sup>, Andrés Tassara<sup>3</sup>, Kamil Erkan<sup>1</sup>, Christopher  
Jekeli<sup>1</sup>, Alexander Braun<sup>4</sup>, Chungyen Kuo<sup>5</sup>,  
Hyongki Lee<sup>6</sup>, Dah-Ning Yuan<sup>7</sup>

<sup>1</sup>Division of Geodetic Science, School of Earth Sciences, Ohio State University,  
Columbus, OH, USA

<sup>2</sup>Department of Geosciences, Princeton University, Princeton, NJ, USA

<sup>3</sup>Departamento de Ciencias de la Tierra, Universidad de Concepción, Concepción, Chile

<sup>4</sup>Department of Geosciences, The University of Texas at Dallas, TX, USA

<sup>5</sup>Department of Geomatics, National Cheng-Kung University, Taiwan

<sup>6</sup>Department of Civil and Environmental Engineering, University of Houston, Houston,  
TX, USA

<sup>7</sup>Jet Propulsion Laboratory, California Institute of Technology, CA, USA

**Corresponding Author:** Lei Wang, Division of Geodetic Science, School of Earth  
Sciences, Ohio State University, 275 Mendenhall Lab., 125 S. Oval Mall, Columbus,  
Ohio 43210, USA. Tel: +1-614-390-7367, [wang.1115@buckeyemail.osu.edu](mailto:wang.1115@buckeyemail.osu.edu)

## **Abstract**

The 27 February 2010 Mw 8.8 Maule, Chile earthquake ruptured over 500 km along a mature seismic gap between 34°S and 38°S – the Concepción-Constitución gap, where no large megathrust earthquakes had occurred since the 1835 Mw ~8.5 event. Notable discrepancies exist in slip distribution and moment magnitude estimated by various models inverted using traditional observations such as teleseismic networks, coastal/river markers, tsunami sensors, Global Positioning System (GPS) and Interferometric Synthetic Aperture Radar (InSAR). We conduct a spatio-spectral localization analysis, based on Slepian basis functions, of data from Gravity Recovery And Climate Experiment (GRACE) to extract coseismic gravity change signals of the Maule earthquake with improved spatial resolution (350 km half-wavelength). Our results reveal discernable differences in the average slip between the GRACE observation and predictions from various coseismic models. The sensitivity analysis reveals that GRACE observation is sensitive to size of the fault, but unable to separate depth and slip. Here we assume depth of the fault is known, and simultaneously invert for the fault-plane area and the average slip using the simulated annealing algorithm. Our GRACE-inverted fault plane length and width are  $429 \pm 6$  km,  $146 \pm 5$  km, respectively. The estimated slip is  $8.1 \pm 1.2$  m, indicating that most of the strain accumulated since 1835 in the Concepción-Constitución gap was released by the 2010 Maule earthquake.

**Keyword: Maule earthquake; Geodynamics; GRACE**

## **1. Introduction**

The 2010 Maule Chilean earthquake, which was caused by the subduction of the Nazca plate underneath the overlying South America plate, is the sixth largest event in the seismic record. Fig. 1 shows the tectonic setting of the Andean subduction zone, and prior significant earthquakes around the Constitución gap (Beck et al., 1998; Campos et al., 2002; Moreno et al., 2008; Nishenko, 1985; Ruegg et al., 2002, 2009) since the 1835 Mw ~8.5 event (Darwin, 1845). The 1906 Mw 8.4, 1943 Mw 7.9 and 1985 Mw 7.8 earthquakes reduced the accumulated stresses in the segments north of the Constitución gap. The slip distribution of the 1960 Mw 9.5 event, the largest earthquake on record, extended north beneath the Arauco peninsula, accompanying stress release south of the gap. The middle locked zone (Constitución gap) had accumulated stresses for 175 years since 1835 until the 2010 Maule event, during which the rupture front propagated mostly upward (trench-ward) and bilaterally (northward and southward) rupturing a 500 km long segment of the megathrust.

Data from teleseismic networks, coastal/river markers, tsunami sensors, Global Positioning System (GPS), and Interferometric Synthetic Aperture Radar (InSAR), have been used to observe and model the coseismic signature and slip history of this devastating event (Delouis et al., 2010; Farías et al., 2010; Lay et al., 2010; Lorito et al., 2011; Moreno et al., 2010; Tong et al., 2010; Vigny et al., 2011). In addition, spaceborne gravimetry data from GRACE (Tapley et al., 2004) have been used to observe coseismic signature of the 2010 Maule earthquake (Heki and Matsuo, 2010; Han et al., 2010) with different spatial resolutions, either based on global spherical-harmonic analysis with additional filtering and decorrelation to remove high-frequency errors

(Heki and Matsuo, 2010) or regional solutions directly using GRACE inter-satellite tracking data at 500 km spatial resolution (Han et al., 2010). Our approach uses spatio-spectral localization with Slepian basis functions (Simons et al., 2006). The spherical Slepian basis, a set of bandlimited functions that have the majority of their energy concentrated by optimization inside of an arbitrarily defined region, provides an efficient method for the analysis and isolation of coseismic gravity signatures and other spatio-spectrally localized geophysical signals (Simons et al., 2006, 2009).

While the slip distribution for the Maule earthquake has been modeled either seismically by analyzing teleseismic records (Lay et al., 2010) or inverted using geodetic measurements including GPS and InSAR (Delouis et al., 2010; Lorito et al., 2010; Tong et al., 2010; Vigny et al., 2011), non-negligible discrepancies exist in the inverted fault parameters from these studies. The discrepancies can be attributed to the following factors. Seismic and geologic data often do not completely constrain the fault geometry, particularly when the primary fault rupture does not reach Earth's surface. Determination of fault geometry often relies on aftershock distribution, which is complex: substantial aftershock activities often occur off the principal fault plane (Segall and Davis, 1997). Geodetic methods, including GPS and InSAR-derived crustal displacements over land, often deployed in the far-field of an undersea earthquake, still play an important role in elucidating the geometry of the rupture. However, for undersea earthquakes, geodetic inversion tends to underestimate the slip due to lack of near-field offshore observation. In contrast, gravitational data are sensitive to deformation either on land or on the seafloor, in the continental or oceanic crust and upper mantle, although the signal-to-noise ratio, particularly in oceanic settings, depends on the size of rupture. The question of interest is whether or not spaceborne gravimetry from GRACE may provide complementary constraints to aid fault inversion.

Although previous studies reported observing coseismic and postseismic deformation of recent great earthquakes by spaceborne gravimetry (Chen et al., 2007; Han et al., 2006, 2008, 2010; Heki and Matsuo, 2010; de Linage et al., 2009; Panet et al., 2007), none of them considered inverting the detected signals for fault parameters. Cambiotti et al. (2011) used GRACE observation to constrain fault depth by five point-like seismic sources for the 2004 Sumatra-Andaman earthquake. However, despite of its coarse spatial resolution, GRACE is still sensitive to the actual dimension of the large rupture of  $\sim 1000$  km by 150 km. It is uncertain that the depth of point source could fully characterize the depths of actual ruptures distributed over a 150 km wide fault plane. Our study not only analyzes the sensitivity of coseismic gravity changes from spaceborne gravimetry to fault parameters, but attempts to use GRACE observations to constrain fault geometry and the average slip for the 2010 Mw 8.8 Maule event.

The organization of the paper after Section 1 (Introduction) is as follows. In Section 2, we will first introduce our spatio-spectral localization method, which uses spherical Slepian basis functions to enable the analysis and isolation of coseismic gravity change signals. This method, jointly with time-series analyses and statistical tests, is then applied to the GRACE monthly gravity-field solutions to extract the coseismic gravity changes resulting from the 2010 Mw 8.8 Maule earthquake. In Section 3, we compare four published slip models, which are derived either from teleseismic records or geodetic measurements (GPS or InSAR). We identify notable discrepancies in various fault parameters among these available models. In order to investigate whether GRACE observations can provide constraints for fault inversion, we further analyze the sensitivity of coseismic gravity changes (at GRACE spatial resolution, estimated at 350 km half-wavelength) to parameters such as fault length, width, depth and average slip. A nonlinear inversion technique, the simulated annealing algorithm

(Kirkpatrick et al., 1983; Pincus 1970), is applied to simultaneously invert for the fault length, width and average slip using coseismic gravity change observables from GRACE. In Section 4, we discuss the inversion results and the associated geophysical analysis.

## **2. Spatio-spectral localization analysis of GRACE data**

### *2.1 Localization using Slepian basis functions to enhance spatio-spectral signals*

The Slepian functions are a family of band-limited spherical-harmonic expansions (to maximal degree  $L$ ) that have the majority of their energy in the space domain concentrated within an arbitrary region  $R$  on the unit sphere  $\Omega$ . They are orthonormal over the whole sphere  $\Omega$  while at the same time orthogonal over the specified concentration region  $R$ , and are obtained either by solving a symmetric matrix-eigenvalue problem in the spectral domain or a Fredholm-integral eigenvalue equation in the spatial domain (Simons et al., 2006). In both cases the eigenvalues ( $0 < \lambda < 1$ ) are a measure of the spatial energy concentration of the corresponding Slepian eigenfunctions, relative to the entire sphere. The spherical Shannon number,  $N$ , which is equal to the sum of the eigenvalues, is an approximation of the number of eigenfunctions that are mostly concentrated in the region. To give some examples for the Slepian bases, Supplementary Fig. 1 shows the first 9 band-limited (maximum degree  $L = 60$ ) Slepian basis functions for the circularly symmetric region with a radius  $\theta = 10^\circ$  centered offshore Chile on the epicenter of the 2010 Maule earthquake. Their eigenvalues  $\lambda$  are all very close to unity indicating nearly perfect spatial concentration despite the limited bandwidth.

The Slepian functions are given by the linear combination of spherical harmonics,

$$g(\vec{r}) = \sum_{l=0}^L \sum_{m=-l}^l g_{lm} Y_{lm}(\vec{r}) \quad (1)$$

subject to the condition

$$\lambda = \frac{\int_R g^2(\vec{r}) d\Omega}{\int_{\Omega} g^2(\vec{r}) d\Omega} = \text{maximum} \quad (2)$$

Maximization of equation (2) generates a homogeneous Fredholm integral equation in the space domain, whose solutions are  $(L+1)^2$

Slepian eigenfunctions  $g_{\alpha}(\vec{r})$  :

$$g_{\alpha}(\vec{r}) = \sum_{l=0}^L \sum_{m=-l}^l g_{\alpha,lm} Y_{lm}(\vec{r}), \quad \text{where } \alpha = 1, 2, \dots, (L+1)^2. \quad (3)$$

After sorting the eigenvalues  $\lambda$  in decreasing order,  $\alpha$  is the rank of the Slepian basis functions in the sorted sequence.

The band-limited monthly geopotential field solutions from GRACE can be represented in the spherical harmonic basis,  $Y_{lm}(\vec{r})$ , or, equivalently, in a Slepian basis,  $g_{\alpha}(\vec{r})$ , of the same bandwidth  $L$ . The equivalence is exact when the same number,  $(L+1)^2$ , of functions is being used. However, when the signal of interest,  $s(\vec{r})$ , is spatially localized, and the Slepian basis is designed to be concentrated inside a corresponding target region, the signal can be very well approximated by a truncated Slepian expansion limited to the first  $N$  terms:

$$s(\vec{r}) = \sum_{l=0}^L \sum_{m=-l}^l s_{lm} Y_{lm}(\vec{r}) = \sum_{\alpha=1}^{(L+1)^2} s_{\alpha} g_{\alpha}(\vec{r}) \approx \sum_{\alpha=1}^N s_{\alpha} g_{\alpha}(\vec{r}), \quad (4)$$

since the first  $N$  Slepian basis functions have almost all of their energy in the concentration region, while the remaining  $(L+1)^2 - N$  basis functions are concentrated outside of it. In equation (4), the spherical harmonics and the corresponding expansion coefficients are indexed by the integer degree  $l$  and order  $m$ , and the Slepian basis functions and expansion coefficients by the linear index  $\alpha$ . The basis transformation leading to the second equality in equation (4) is unitary.

For illustration we expand the coseismic gravity change predicted from a seismically derived fault model by the United States Geological Survey, USGS (2010), up to degree and order 100 using both spherical harmonics and Slepian functions with the same bandwidth. Fig. 2a shows the coseismic gravity changes represented using all 10201 spherical harmonic coefficients. Fig. 2d reveals that among those only 5598 coefficients are significant contributors to the signal, in that they have absolute values that are larger than one hundredth of the maximum of the entire set. Fig. 2b shows the approximation of the same coseismic gravity changes, but only using the first  $N = 77$  best-localized Slepian functions in the expansion. Compared to Fig. 2a, the coseismic gravity changes inside of the concentration region are extremely well captured by the partial sum of the first  $N = 77$  terms in the Slepian expansion, since only 50, belonging to those with the highest concentration ratios, have significant values, as shown in Fig. 2e. Fig. 2c shows the differences between the representations in Fig. 2a and Fig. 2b. This is one of the advantages of making expansions in the Slepian basis: band-limited geophysical signals that are regional in nature are sparse in this sense (Simons et al., 2009). The root-mean-squared (rms) misfit of the expansions shown in Fig. 2a and Fig. 2b is 0.05% of the rms of the signal when calculated over the entire sphere, and 0.14% of the signal rms when calculated over the circular concentration region.

In addition to achieving sparsity in the representation of local signals, the top-ranked Slepian basis functions on circular concentration regions, fortuitously, match the patterns themselves of the geopotential perturbation generated by coseismic deformation. Using normal-mode theory, Simons et al. (2009) showed that the first-order Eulerian gravitational potential perturbations in a spherically-symmetric non-rotating Earth due to a variety of earthquake focal-mechanism end-members corresponding to monopole, dipole, and quadrupole sources,

form patterns that are similar to the shape of some of the best-concentrated Slepian functions on symmetric spherical caps, e.g. see the panels corresponding to Supplementary Fig. 1a-e. This is an additional advantage by which the Slepian basis functions are particularly suitable to represent coseismic gravity changes from moment-tensor point-source earthquakes.

## *2.2 GRACE data processing*

Here we use localized analysis with Slepian basis function to enhance the spatial resolution and the signal-to-noise ratio of the GRACE-observed coseismic gravity-change signal associated with the 2010 Maule Chilean earthquake. In this study, ninety-one GRACE Level 2 Release 04 geopotential fields from the Center for Space Research (CSR), spanning from January 2003 to August 2010, were used for analysis. These solutions, one for every month, consist of spherical harmonic coefficients up to degree and order 60, corresponding to a maximum resolution of 333 km (half-wavelength). Here in order to preserve the maximum spatial resolution, we did not decorrelate or filter the monthly Stokes coefficients (e.g., as done by Heki and Matsuo, 2010), in favor of using Slepian-function based localization to enhance or retain the resolution of the GRACE observations, estimated at  $\sim 350$  km resolution.

A circularly symmetric cap of radius  $10^\circ$  is chosen as the concentration region. To properly choose the center of concentration region, we check the behavior of the time series of the Slepian coefficients as a function of the concentration center location. The concentration center is moved along a west-east profile across the epicenter, and the Slepian transformations are applied to GRACE geopotential fields every  $0.5^\circ$  on the profile. From the resulting Slepian coefficients obtained at different concentration centers, a constant term, a linear trend, the first six largest periodic components and a step

function between the months of February and March 2010 were simultaneously fitted by least-squares adjustment.

In addition, the Student  $t$ -test is applied to check whether the estimated step functions, which are considered to be coseismic signals, are statistically significant. Fig. 3 shows the estimated step values (Fig. 3a) and the corresponding  $t$ -values (Fig. 3b) from the 1<sup>st</sup> and 3<sup>rd</sup> Slepian coefficient series as a function of concentration center location. No significant step is detected in other coefficients. This is not hard to understand. The strike of fault is about 19°, which is close to zero. The predicted coseismic gravity change, as shown in Fig. 2a, clearly shows the ‘dipole shaped’ spatial pattern, i.e., negative gravity signal on the land, and positive signal over the ocean. However, the 2<sup>nd</sup> Slepian function (Supplementary Fig.1b) has negative signal over the north and positive signal above the south, which is less correlated with the spatial pattern of the gravity change of Maule earthquake. The 5<sup>th</sup> Slepian function (Supplementary Fig. 1e) matches the spatial pattern of the gravity changes caused by strike-slip. However, the strike-slip component is one order of magnitude smaller than the thrust component for Maule earthquake (Tong et al., 2011), and thus cannot be detected by GRACE with its current accuracy.

Fig. 3b shows that the estimated steps in the time series of the 1<sup>st</sup> Slepian coefficients are statistically significant within much of the range of the concentration centers, thus fulfilling a 95% confidence criterion ( $t = 1.99$ ). The estimated step values achieve maximum value when the concentration center is located at (69.9°W, 35.8°S), which is a point as far as almost 3° east of the earthquake epicenter. Although the jump in the time series of the 1<sup>st</sup> expansion coefficient is more pronounced when the concentration center moves eastwards from the epicenter, this comes at the expense of the 3<sup>rd</sup> coefficient, for which no other significant jumps can be detected. Fig. 3b shows that the fitted step value in the 3<sup>rd</sup> Slepian coefficients are statistically significant (95% confidence level) only if the concentration center resides between 72.9°W and 70.9°W. If the concentration center moves eastwards further beyond 70.9°W, all the estimated step values in the 3<sup>rd</sup> coefficient become insignificant.

Fig. 4 explicitly shows the original and fitted time series when the concentration centers are located at (72.9°W, 35.8°S) and (69.9°W, 35.8°S), respectively.

Thus, in order to keep both significant jumps in the 1<sup>st</sup> and 3<sup>rd</sup> Slepian coefficient series and, meanwhile, to make sure that the concentration center is not too far from the epicenter, we choose the center of the concentration region at the mid point (71.9°W, 35.8°S) of the range between 72.9°W and 70.9°W, where both estimated step values in the 1<sup>st</sup> and 3<sup>rd</sup> Slepian coefficients are statistically significant. We use the step functions fitted from the 1<sup>st</sup> and 3<sup>rd</sup> functions to finally estimate the coseismic gravity changes. The results are shown in Fig. 5.

The peak value in the negative signal on land from GRACE observation is  $\sim -8.0$   $\mu\text{Gal}$  and the maximum positive signal is  $\sim 1.2$   $\mu\text{Gal}$  over the ocean. It should be realized that our GRACE observation only consists of the 1<sup>st</sup> and 3<sup>rd</sup> Slepian basis functions, for which significant jumps (induced by earthquake) can be detected. Figure 6 shows how well the representation using only the 1<sup>st</sup> and 3<sup>rd</sup> Slepian basis functions can approximate the original signal. The partial representation using only 1<sup>st</sup> and 3<sup>rd</sup> Slepian functions in Fig. 6b resolves almost all of the negative signals in the full-resolution model (Fig. 6a) on land, but over the ocean, the detailed signatures of coseismic gravity change cannot be exactly represented by the 1<sup>st</sup> and 3<sup>rd</sup> Slepian bases alone (Fig. 6c). Since only the 1<sup>st</sup> and 3<sup>rd</sup> Slepian functions together do not form a complete basis for the space of bandlimited functions, more Slepian basis functions must be involved if one wants to obtain an accurate signal in the ocean, which has a more intricate spatial pattern than the signal on land. We find that the GRACE observed earthquake-induced step-function is significant only in the 1<sup>st</sup> and 3<sup>rd</sup> Slepian coefficients. This is well explained by the observation that, since the positive signal over the ocean due to sea-floor uplift is only  $\sim 1$   $\mu\text{Gal}$  at GRACE spatial resolution, this is close to the GRACE error level. We can thus state with

confidence that the GRACE observations shown in Fig. 5 resolve almost all the negative signals over land caused by the Maule earthquake, while the detected positive signals over the ocean qualitatively correspond to seafloor uplift, but should not be quantitatively applied in the inversion.

### **3. Estimation of fault parameters from GRACE observations**

#### *3.1 Comparisons of current slip models*

Reliable estimation of coseismic earthquake slip is necessary to evaluate the pre-locking status and the level of stress release. However, existing slip models obtained by various constraints or via inversion of observations, including uplifted/subsided biomarkers, teleseismic data, InSAR, GPS, and tsunami observations, exhibit notable differences, both in slip amplitude and distribution. Here we compare four published slip models: Model I is a finite-fault solution derived from seismic observations (USGS, 2010); Model II is an inversion using teleseismic  $P$  and  $SH$  waves (Lay et al., 2010); Model III is an inversion based on InSAR interferograms and GPS displacement measurements (Tong et al., 2010); and Model IV is derived by combining land-level changes from coastal bio-markers, InSAR deformation, GPS displacement and tsunami observations at tide-gauges and DART buoys (Lorito et al., 2011). Inset plots in Fig. 1 show the maps of the finite-fault slip distributions from these models, while Table 1 compares some key parameters. As can be seen from Table 1, other than the obvious discrepancies in the length and width of the fault plane, the difference in the predicted maximum slips between the four models is as large as  $\sim 13$  m, and the difference in the fault depth ranges up to 6 km. Significant discrepancies also can be found in the potency, the integral of the slip over the rupture surface (Ben-Menahem & Singh, 1981). Moreover, the slip distributions predicted by these models have large discrepancies. While Model I predicts more slip in the southern asperities, larger slips are concentrated to the north of the epicenter in Models II, III and IV (Fig. 1). The last row in Table 1

also lists the fault parameters inverted in this study from GRACE observation, which will be discussed further below.

Coseismic gravity changes can be computed from slip models, since coseismic slip due to the sudden unlocking of the megathrust causes an instantaneous elastic rebound of the upper plate, which translates into a distinctive pattern of uplift and subsidence at the surface and induces dilatation of the formerly compressed forearc volume. Assuming an elastic half-space, we use all four models to predict the coseismic gravity changes due to the effects of coseismic deformation including both the single-layer topographical change (uplift/subsidence) of the seafloor and the internal density changes (contraction/expansion) within the crust and upper mantle (Okubo, 1992). To make the model predictions commensurate with the approximate spatial resolution of the GRACE observations, all the model predictions, which are originally modeled with  $0.25^\circ \times 0.25^\circ$  grid at full resolution, are truncated to degree 60, and an isotropic Gaussian filter (Jekeli, 1981; Wahr et al., 1998) with a smoothing radius of 350 km is applied. The results are shown in Fig. 7.

The spatial patterns of total gravity change predicted from all four slip models (Fig. 7a, d, g and j), which are the summations of the effects due to surface vertical deformation (Fig. 7b, e, h and k) and internal dilatation (Fig. 7c, f, i and l), are similar at the spatial resolution attainable by GRACE observations, and consistent with the GRACE-detected gravity changes (Fig. 5), even though Model I places more slip in the southern asperities, whereas Models II, III and IV have larger slip north of the epicenter. All model predictions indicate apparent negative gravity changes on land east of the epicenter. Hence, we conclude that GRACE is not sensitive to the detailed slip distribution of the 2010 Chilean shock, mainly because the length of faulting is of the same order of magnitude as the limiting resolution of the GRACE data.

Although the coseismic gravity changes predicted by the models

exhibit similar spatial patterns, the amplitudes from the four models are discernably different. Peak values in the negative signals on land predicted by Models I–IV are  $-8.1 \mu\text{Gal}$ ,  $-8.8 \mu\text{Gal}$ ,  $-6.9 \mu\text{Gal}$  and  $-9.0 \mu\text{Gal}$ , respectively (Fig. 7). Since the four models give different slip amplitudes, they proportionally lead to different amplitude in the predicted coseismic gravity change. Although both Models I & II are derived from teleseismic wave analysis, the maximum slip amplitudes are 14.6 m and 27.8 m respectively, presumably because of different model assumptions and data distributions, as well as different intrinsic ranges of apparent velocities in the observations (Lay et al., 2010). Both Models III and IV inverted data from land-based InSAR deformation and GPS displacement measurements. Model III, which has a maximum slip of 18 m, probably underestimates the amount of slip at shallower depth as a consequence of lacking offshore observations (Tong et al., 2010). Using tsunami observations to further constrain the offshore displacement, Model IV provides a larger estimate of 18.8 m as the peak value in slip.

GRACE-detected gravity changes, which peak at  $-7.9 \mu\text{Gal}$  over land, are compared with Model predictions on three profiles along latitudes  $32^\circ\text{S}$ ,  $36^\circ\text{S}$  and  $39^\circ\text{S}$  (Fig. 8). The grey lines in Fig. 5 indicate these profiles. Although both Models III and IV used the same InSAR data, they provide the smallest and largest magnitudes of gravity changes, respectively, among the GRACE observation and the models, along all three profiles (Fig. 8). The large discrepancy between these two models can probably be attributed to the fact that the tsunami observations are used in Model IV to estimate the offshore displacement. The amplitudes of predicted gravity changes by seismically derived models (Models I and II) generally reside in the extent bounded by Models III and IV. Along the  $32^\circ\text{S}$  and  $36^\circ\text{S}$  profiles, GRACE observations have peak values around longitude  $70^\circ\text{W}$ , and they are approximately equal to the means of the model predicted maximum

amplitudes. However, to the south of the rupture along 39°S profile, the GRACE-observed gravity change, which is of the same order of magnitude as the prediction from Model IV, is relatively larger than the predictions from Models I, II, and III.

Since there is no *a priori* error information available for the observation, we choose to use the model error (*a posteriori* error estimation) to provide error information for our GRACE observation. Since the earthquake-induced jumps are fitted from the time series of the 1<sup>st</sup> and 3<sup>rd</sup> Slepian coefficients by least-squares adjustment, we can estimate the data variance from the residuals in the time series, and thence the variance of the fitted jumps. The blue shadings along with the GRACE observation profiles in Fig. 8 indicate the estimated model errors based on this procedure. We conclude that the GRACE-derived amplitudes can be used to independently constrain the fault parameters of the Maule earthquake, since these are discernibly different from the amplitudes derived by other coseismic slip models.

### 3.2 Sensitivity analysis

We now analyze the sensitivity of the coseismic gravity changes to various fault parameters. A finite fault plane is set with length, depth, dip, strike and rake fixed at 500 km, 4 km, 15°, 19°, and 90°, respectively. The width of the fault plane is made to vary between 150 km and 200 km in steps of 50 km, and the uniform slip on the fault plane varies from 6 m to 10 m for each width value. Along an east-west profile across the middle of the fault plane, the coseismic gravity changes for each case are shown in Fig. 9 (left). We can see from Fig. 9 (left) that when the width of the fault plane is 150 km, 200 km, or 250 km, the trough values of the predicted gravity change on the profile occur around longitudes -70.4°, -69.4°; and -68.8°, respectively. In other words, with increasing of fault-plane width, the location of the minimum in the observed gravity change moves to the east. Moreover, for a fixed

width, the amplitude of the predicted gravity change increases proportionally with slip amplitude. Therefore, the location and amplitude of the minimum value in the coseismic gravity observation, i.e., the shape/size of the observed gravity profile, provide constraints on the width of the fault plane and its average slip.

Fig. 10 gives a map view to further show the sensitivity of coseismic gravity changes to fault width and length. As in the previous example, the fault dip, strike and rake are fixed to be  $15^\circ$ ,  $19^\circ$ , and  $90^\circ$ , respectively. The upper edge of the fault is set at 5 km depth, and the slip is uniformly fixed at 7 m. The width of the fault plane is set to be 50 km, 150 km and 250 km, respectively, and for each fixed width, the coseismic gravity changes are computed for fault lengths of 300 km, 600 km and 900 km. For certain fixed fault lengths, the location of the negative peak in the predicted coseismic gravity changes moves eastwards with increased fault width. For fixed fault width, the spatial pattern of the gravity changes becomes more elongated in the north-south direction as the fault length grows.

Although GRACE detected coseismic gravity change is sensitive to fault length, width and average slip, there is trade-off between fault depth and average slip. To show this, a fault plane (length, width, dip, strike and rake are fixed to be 500 km, 150 km,  $15^\circ$ ,  $19^\circ$ , and  $90^\circ$  respectively) is placed at depth (measured down to the upper edge of the fault) of 4 km, 5 km and 6 km, respectively. At each depth, the coseismic gravity changes are computed with slip of 6 m, 7 m, 8 m and 9 m, respectively. Fig. 9 (right) shows the gravity changes along the same profile as in Fig. 9 (left). We can clearly see the trade-off between the depth and slip. To be specific, at a spatial resolution of 350 km, the coseismic gravity changes given by a fault at a depth of 4 km and slip of 9 m are similar to the ones computed from a fault at a depth of 6 km and slip of 8.5 m. For the depth range from 4 km to 6 km in this case, the trade-off between depth and slip would cause maximum errors of

~0.5 m in the slip estimation using coseismic gravity changes only. Thus, for the Maule earthquake, the coseismic gravity changes observed by GRACE add little constraint to the depth estimation for the fault plane. The depth information estimated from other observations (e.g. seismic or geodetic observations) should be used in order to invert GRACE-derived observations for other fault parameters.

### *3.3 Inverting for fault parameters from GRACE observations*

Here, we use the GRACE observations to invert for fault parameters. A simplified elastic model with uniform slip on the fault plane is assumed for the study. Here we fix the strike angles to be  $19^\circ$  as given by the global CMT solutions (GCMT, 2011). We assume a uniform dip of  $15^\circ$ , which is consistent with the dip angle used by Vigny et al. (2011). By jointly inverting the continuous GPS, survey GPS and InSAR observations, Vigny et al (2011) suggested that the rupture started from 5 km depth along the megathrust interface. Therefore, we choose the depth to the top edge of the fault as 5 km. Based on previous analysis, even if there is  $\pm 1$  km uncertainty in depth value, the trade-off effect in the slip estimate should be less than 0.5 m. The rake angle is fixed as  $90^\circ$  in our inversion, i.e., we only invert for the thrust component and neglect the right-lateral strike slip component. This simplification can be justified by following two points: first, as shown by Tong et al. (2010), the strike-slip seismic moment is one order of magnitude smaller than the thrust (dip-slip) seismic moment; secondly, there is no significant jump detected in the time series of the coefficient associated to the 5th Slepian basis function (Supplementary Fig. 1e), whose shape matches the spatial pattern of the coseismic gravity changes due to strike slip motion.

A simulated annealing algorithm is applied to simultaneously estimate fault-plane length, width and slip on the fault. Simulated annealing (SA) is a popular non-uniform Monte Carlo method for global

optimization, and has been successfully applied across several disciplines, including geophysical inversion (Kirkpatrick et al., 1983; Pincus, 1970). The power of SA is that it can be used in cases where the model-data relationship is highly non-linear and the objective function has many local minima. In addition, it avoids searching the state-space uniformly, thereby limiting the computational demands. By analogy with annealing in thermodynamics, the algorithm begins at a high effective temperature, and is slowly 'cooled' until the system 'freezes' and no further changes occur, i.e., the system arrives at the minimum-energy state.

We apply the SA algorithm by defining the cost function (energy function) as the sum of squares of the differences between GRACE-observed gravity changes and model predictions on three profiles along latitudes 32°S, 36°S, and 39°S (Fig. 5). The state space consists of the length, width and average slip. Supplementary Figs. 2a-c show the histograms of the accepted samplings for fault length, width and slip after convergence of the iterations. The ultimate optimal estimate for fault length, width and slip are, 429 km, 146 km, and 8.1 m, respectively. In order to further investigate parameter uncertainties induced by GRACE observation errors, we also use the lower and upper bounds of the *a posteriori* error estimates for the GRACE observations to invert for fault-plane width, length and average slip. At the lower bound (shaded light blue in Fig. 8) the algorithm converges to a fault plane with length 430 km, width 143 km, and average slip of 9.1 m (see Supplementary Figs. 2 d- f for the histograms of the solutions), while using the upper bound of the GRACE data yields estimates of fault-plane length, width and average slip of 427 km, 149 km and 7.1 m, respectively. Similarly, Supplementary Figs. 2g-i shows the converged fault length, width and slip estimates at the end of iteration. The maximum widths of the global minimum in state space for above three inversions are 8 km, 4 km and 0.3 m for length, width and slip,

respectively.

We finally estimate the fault length and width as  $429 \pm 6$  km,  $146 \pm 5$  km, respectively, and the average slip as  $8.1 \pm 1.2$  m. Assuming a mean rigidity of 33 GPa (Vigny et al. 2011), the new GRACE-derived total seismic moment is  $1.67 \times 10^{22}$  Nm, resulting in a moment-magnitude  $M_w$  8.75, which is comparable to contemporary solutions ( $M_w$  8.8). Since the rake is fixed as  $90^\circ$  in the inversion, our estimated  $M_w$  8.75 value only corresponds to the thrust part of the total moment magnitude, although the seismic moment of the strike-slip component is one order of magnitude smaller than that of thrust component.

#### **4. Discussion and conclusions**

The acquisition of information on ruptured fault geometry and co-seismic slip distribution helps one better understand the earthquake mechanism and evaluate the seismic hazard potential after large earthquakes. Due to the intrinsic limitations in fault inversions using either teleseismic records or geodetic measurements, discrepancies exist in published slip models for the  $M_w$  8.8 2010 Maule earthquake. Those translate into uncertainties regarding the assessment of short-term seismic hazard left inside the Concepción-Constitución seismic gap (Moreno et al., 2010; Lorito et al., 2011; Lay, 2011). GRACE has the capability of observing earthquake-induced gravity changes over both ocean and land, and hence potentially provides constraints for long-wavelength offshore deformation for which typical geodetic measurements, such as GPS and InSAR, are not available. Unlike the 2004 Sumatra-Andaman earthquake which ruptured a 1500 km-long and 150 km-wide segment along the Sunda subduction megathrust (Chlieh et al., 2007), and consequently led to more than  $10 \mu\text{Gal}$  positive gravity change in GRACE observation over ocean (Han et al., 2006), the 2010 Maule shock produced positive gravity changes of only  $1 \sim 2 \mu\text{Gal}$  which is close to the error level of GRACE observation. Therefore, owing to the

relatively small rupture size and slip amplitude of the Maule earthquake, the study of its deformation cannot fully take advantage of the aforementioned advantages of GRACE. However, we have demonstrated here that GRACE spaceborne gravimetry is useful to complement seismic and geodetic observations because the total permanent gravity change resulting from great earthquakes observed by GRACE is a distinct and independent observation type.

By investigating the sensitivity of coseismic gravity changes to various fault parameters, we find that variations observed by GRACE cannot identify differences in detailed slip distributions for the 2010 Mw 8.8 Maule earthquake. However, using a simple elastic dislocation model we can estimate uniform average slip, length and width of the rupture interface. Although we noted a tradeoff between average slip and fault depth, fixing the later with independent information (Vigny et al., 2011), we find the amplitude of the observed coseismic gravity change is proportional to the average slip on the fault plane. The location of the minimum value of coseismic gravity change indicates the down-dip limit of the rupture, i.e., the width the fault plane ( $\sim 146$  km), while the south-north extent of the gravity change signature constrains the fault length ( $\sim 429$  km). The dimensions and location of our ruptured fault coincide with the extent of significant co-seismic slip ( $> 2$  m) predicted by published models. Our inversion algorithm estimated an average slip of 8.1 m, which gives a seismic moment ( $1.67 \times 10^{22}$  Nm) and moment-magnitude (Mw 8.75), similar to previous estimations.

Rapid afterslip on the ruptured fault is the predominant post-seismic deformation mechanism and typically occurs over timescales of several months (Perfettini et al., 2010). Afterslip can be attributed to either aseismic slip in the sedimentary layer overlying the fault, coseismic slip generated by aftershocks, or silent slow slip triggered by the mainshock-induced stress and friction changes (Vigny et al. 2011). Because of its temporal resolution of a month, GRACE cannot identify

gravity changes due to these earliest manifestations of post-seismic deformation, and therefore is not able to separate them from the coseismic estimates. By using campaign- and continuous-GPS observations, Vigny et al. (2011) has shown that afterslip on the megathrust interface within 12 days following the main shock accounts for only 4% of the coseismic moment, and the maximum post-seismic slip is estimated to be  $\sim 50$  cm. This lies within the error range of the GRACE-estimated slip provided in the previous section and it seems unlikely that afterslip could seriously contaminate our co-seismic slip estimation.

In the extreme case that the plate interface in Constitución gap has remained fully locked for 175 years between 1835 and 2010, the cumulated slip deficit before the Maule earthquake at a rate of 62–68 mm/yr of plate convergence (Kendrick et al., 2003) would be on the order of 11–12 m. The difference with our estimated average slip could indicate that a remaining slip deficit of 3–4 m could still generate a large earthquake ( $M_w$  8.5 if occurring in the same fault plane of our model) to fully close the gap, supporting the conclusion of Lorito et al. (2011). However, some alternatives must be considered on this limiting case.

GPS-derived velocity fields for the decade before the 2010 Maule earthquake show an overall strong coupling in this region (Khazaradze and Klotz, 2003; Ruegg et al., 2009; Moreno et al., 2010). However, there is no evidence that bears on whether or not the plate interface ever experienced aseismic slip during the interseismic phase before 2000, especially as afterslip after the 1835 earthquake. It has been shown (Perfettini et al., 2010; Ide et al., 2007) that slow or silent slip events during the interseismic and post-seismic phases are common features of subduction-zone megathrusts, and can release large amounts of seismic moment (10-70% of the budget predicted by plate convergence). With the available information, it is impossible to discard such events as potential factors reducing the slip deficit before the Maule earthquake and hence explaining the difference with our average

co-seismic estimation. Moreover, aseismic slip normally occurs on discrete patches of the megathrust, and hence generates a spatially variable distribution of plate locking, which can be imaged by interseismic GPS velocity fields (Moreno et al., 2010; Loveless and Meade, 2011). When computed with the same model for geometry and rheology of the subduction zone, co-seismic slip patches seems to roughly coincide with strongly locked regions over the megathrust, as shown by Moreno et al. (2010) for the Maule event, and by Loveless and Meade (2011) for the 2011 Mw 9 Tohoku-Oki earthquake. GRACE cannot recognize the detailed spatially variable slip distribution, but only the averaged slip over the whole ruptured megathrust. Therefore, it is hard to tell whether or not the Constitución gap is completely closed just from the slip deficit of 3-4 m between GRACE observed average coseismic slip ( $\sim 8$  m) and expected value (11–12 m). However, we conclude that most of the strain accumulated since 1835 in the Concepción-Constitución gap was released by the 2010 Maule earthquake.

Our work demonstrates that spaceborne gravimetry provides an independent and thus valuable constraint on the average co-seismic slip for great megathrust events, although the spatial resolution attained by GRACE does not allow for a distinction of the variable slip distribution. However, the detection of the total gravity change produced by coseismic mass redistributions provides a complementary observation to geodetic measurements available on land. Future studies on simultaneous inversion of both data types could further improve the fidelity of coseismic slip models.

## REFERENCES

1. Beck, S., Barrientos, S., Kausel, E., Reyes, M., 1998. Source characteristics of historic earthquakes along the central Chile subduction zone. *J. S. Am. Earth Sci.* 11, 115-129.
2. Ben-Menahem, A., Singh, S. J., 1981. *Seismic Waves and Sources*, Springer-Verlag, New York.
3. Cambiotti, G., Bordoni, A., Sabadini, R., Colli, L., 2011. GRACE gravity data help constraining seismic models of the 2004 Sumatran earthquake. *J. Geophys. Res.*, 116, B10403.
4. Campos, J., Hatzfeld, D., Madariaga, R., Lopez, G., Kausel, E., Zollo, A., Iannaccone, G., Fromm, R., Barrientos, S., Lyon-Caen, H., 2002. A seismological study of the 1835 seismic gap in south-central Chile. *Phys. Earth Planet. Int.* 132, 177-195.

5. Chen, J. L., Wilson, C. R., Tapley, B. D., Grand, S., 2007. GRACE detects coseismic and postseismic deformation from the Sumatra-Andaman earthquake. *Geophys. Res. Lett.* 34, L13302.
6. Chlieh, M., Avouac, J. P., Hjorleifsdottir, V., Song, T. R. A., Ji, C., Sieh, K., Sladen, A., Hebert, H., Prawirodirdjo, L., Bock, Y., Galetzka, J., 2007. Coseismic slip and afterslip of the great M-w 9.15 Sumatra-Andaman earthquake of 2004. *Bull. Seismol. Soc. Am.*, 97, S152-S173.
7. Darwin, C., 1845. *Journal of the Researches into the Natural History and Geology of the Countries Visited During the Voyage of the HMS Beagle Round the World*, 2<sup>nd</sup> ed., John Murray.
8. de Linage, C., Rivera, L., Hinderer, J., Boy, J. P., Rogister, Y., Lambotte, S., Biancale, R., 2009. Separation of coseismic and postseismic gravity changes for the 2004 Sumatran earthquake from 4.6 yr of GRACE observations and modelling of the coseismic change by normal mode summation. *Geophys. J. Int.* 176, 695–714.
9. Delouis, B., Nocquet, J.-M., Vallée, M., 2010. Slip distribution of the February 27, 2010 Mw = 8.8 Maule Earthquake, central Chile, from static and high-rate GPS, InSAR, and broadband teleseismic data. *Geophys. Res. Lett.* 37, L17305.
10. Farías, M., Vargas, G., Tassara, A., Carretier, S., Baize, S., Melnick, D., Bataille, K., 2010. Land-level changes produced by the Mw 8.8 2010 Chilean Earthquake. *Science* 329, 916.
11. Han, S. C., Shum, C. K., Bevis, M., Ji, C., Kuo C. Y., 2006. Crustal dilatation observed by GRACE after the 2004 Sumatra-Andaman earthquake. *Science* 313(5787), 658–666.
12. Han, S.-C., Simons, F., 2008. Spatiospectral localization of global geopotential fields from the Gravity Recovery and Climate Experiment (GRACE) reveals the coseismic gravity change owing to the 2004 Sumatra-Andaman earthquake. *J. Geophys. Res.* 113, B01405.
13. Han, S.-C., Sauber, J., Luthcke, S., 2010. Regional gravity decrease after the 2010 Maule (Chile) earthquake indicates large-scale mass redistribution. *Geophys. Res. Lett.* 37, L23307.
14. Heki, K., Matsuo, K., 2010. Coseismic gravity changes of the 2010 earthquake in central Chile from satellite gravimetry. *Geophys. Res. Lett.* 37, L24306.
15. Ide, S., Beroza, G. C., Shelly, D. R., Uchide, T., 2007. A scaling law for slow earthquakes. *Nature* 447, 76-79.
16. Jekeli, C., 1981. Alternative methods to smooth the Earth's gravity field. Rep. 327, Dep. of Geod. Sci. and Surv., Ohio State Univ., Columbus.
17. Khazaradze, G., Klotz, J., 2003. Short and Long-term effects of GPS measured crustal deformation rates along the South-Central Andes. *J. Geophys. Res.* 108 (B4), 1-13.

18. Kirkpatrick, S., Gelatt, C. D. Jr., Vecchi, M.P., 1983. Optimization by simulated annealing. *Science* 220, 671-680.
19. Lay, T., Ammon, C. J., Kanamori, H., Koper, K. D., Sufri, O., Hutko, A. R., 2010. Teleseismic inversion for rupture process of the 27 February 2010 Chile (Mw 8.8) earthquake. *Geophys. Res. Lett.* 37, L13301.
20. Lay, T., 2011. A Chilean surprise. *Nature* 471, 174-175.
21. Lorito, S., Romano, F., Atzori, S., Tong, X., Avallone, A., McCloskey, J., Cocco, M., Boschi, E., Piatanesi, A., 2011. Limited overlap between the seismic gap and coseismic slip of the great 2010 Chile earthquake. *Nature Geoscience* 4, 173-177.
22. Loveless, J. P., and Meade, B. J., 2011. Spatial correlation of interseismic coupling and coseismic rupture extent of the 2011 Mw = 9.0 Tohoku-oki earthquake. *Geophys. Res. Lett.* 38, L17306.
23. Moreno, M. S., Klotz, J., Melnick, D., Echtler, H., Bataille, K., 2008. Active faulting and heterogeneous deformation across a megathrust segment boundary from GPS data, south central Chile (36-39°S). *Geochem. Geophys. Geosyst.* 9, Q12024.
24. Moreno, M., Rosenau, M., Oncken O., 2010. Maule earthquake slip correlates with pre-seismic locking of Andean subduction zone. *Nature* 467, 198-202.
25. Nishenko, S.P., 1985. Seismic potential for large and great interplate earthquakes along the Chilean and Southern Peruvian Margins of South America: A quantitative reappraisal. *J. Geophys. Res.* 90, 3589-3615.
26. Okubo, S., 1992. Potential and gravity changes due to shear and tensile faults in a half-space. *J. Geophys. Res.* 97, 7137-7144.
27. Panet, I., Mikhailov, V., Diament, M., Pollitz, F., King, G., de Viron, O., Holschneider, M., Biancale, R., Lemoine, J.-M., 2007. Coseismic and post-seismic signatures of the Sumatra 2004 December and 2005 March earthquakes in GRACE satellite gravity. *Geophys. J. Int.* 171, 177-190.
28. Perfettini, H., Avouac, J. P., Traverza, H., Kositsy, A., Nocquet, J. M., Bondoux, F., Chlieh, M., Sladen, A., Audin, L., Farber, D. L., Soler, P., 2010. Seismic and aseismic slip on the Central Peru megathrust. *Nature* 465, 78-81.
29. Pincus, M., 1970. A Monte Carlo method for the approximate solution of certain types of constrained optimization problems. *Oper. Res.* 18, 1225-1228.
30. Ruegg, J. C., Campos, J., Madariaga, R., Kausel, E., de Chabaliere, J. B., Armijo, R., Dimitrov, D., Georgiev, I., Barrientos, S., 2002. Interseismic strain accumulation in south central Chile from GPS measurements, 1996-1999. *Geophys. Res. Lett.* 29, 1517-1520.
31. Ruegg, J. C., Rudloff, A., Vigny, C., Madariaga, R., de Chabaliere, J.B., Campos, J., Kausel, E., Barrientos, S., Dimitrov, D., 2009.

- Interseismic strain accumulation measured by GPS in the seismic gap between Constitución and Concepción in Chile. *Phys. Earth Planet. Int.* 175, 78-85.
32. Segall, P., Davis, J. L., 1997. GPS applications for geodynamics and earthquake studies. *Annual Reviews of Earth and Planetary Science* 25, 301-336.
  33. Simons, F. J., Dahlen, F. A., Wiecek, M. A., 2006. Spatiospectral concentration on a sphere. *SIAM Rev.* 48(3), 504-536.
  34. Simons, F. J., Hawthorne, J. C., Beggan, C. D., 2009. Efficient analysis and representation of geophysical processes using localized spherical basis functions. *Proc. SPIE*, 7446.
  35. Swenson, S., Wahr, J., 2006. Post-processing removal of correlated errors in GRACE data. *Geophys. Res. Lett.* 33, L08402.
  36. Tapley, B. D., Bettadpur, S., Ries, J.C., Thompson, P.F., Watkins, M., 2004. GRACE measurements of mass variability in the earth system science. *Science* 305, 503-505.
  37. Tong, X., Sandwell, D., Luttrell, K., Brooks, B., Bevis, M., Shimada, M., Foster, J., Smalley Jr., R., Parra, H., Báez Soto, J. C., Blanco, M., Kendrick, E., Genrich, J., Caccamise II, D. J., 2010. The 2010 Maule, Chile earthquake: Dwindip rupture limit revealed by space geodesy. *Geophys. Res. Lett.* 37, L24311.
  38. Vigny, C., Socquet, A., Peyrat, S., Ruegg, J.-C., Métois, M., Madariaga, R., Morvan, S., Lancieri, M., Lacassin, R., Campos, J., Carrizo, D., Bejar-Pizarro, M., Barrientos, S., Armijo, R., Aranda, C., Valderas-Bermejo, M.-C., Ortega, I., Bondoux, F., Baize, S., Lyon-Caen, H., Pavez, A., Vilotte, J. P., Bevis, M., Brooks, B., Smalley, R., Parra, H., Baez, J.-C., Blanco, M., Cimbaro, S., and Kendrick, E., 2011. The 2010 Mw 8.8 Maule Megathrust Earthquake of Central Chile, Monitored by GPS. *Science* 332, 1417-1421.
  39. Wahr, J., Molenaar, M., Bryan, F., 1998. Time variability of the Earth's gravity field: Hydrological and oceanic effects and their possible detection using GRACE. *J. Geophys. Res.* 103(B12), 30,205–30,229.
  40. Global Centroid-Moment-Tensor (CMT) project, 2011. <http://www.globalcmt.org>
  41. Finite fault model, U.S. Geological Survey (USGS), 2010. [http://earthquake.usgs.gov/earthquakes/eqinthenews/2010/us2010tfan/finite\\_fault.php](http://earthquake.usgs.gov/earthquakes/eqinthenews/2010/us2010tfan/finite_fault.php)

**Acknowledgment** This research was supported by the U. S. National Science Foundation under Grants EAR-1013333 and EAR-1014606, and partially supported under the Chinese Academy of Sciences/SAFEA International Partnership Program for Creative Research Teams. GRACE data products are from NASA via the University of Texas Center for Space Research and JPL-PODAAC. We thank Chen Ji, UCSB, for providing his coseismic model and also his comments and suggestions, which have enhanced the quality of the manuscript. We thank the modelers for providing their coseismic slip models used in the study. We thank the Editor and two anonymous reviewers for providing constructive comments, which resulted in the improvement of the manuscript.

## Table Caption

**Table 1:** Comparisons of key characteristics in the finite-fault models of Model I by USGS (2010), Model II by Lay et al. (2010), Model III by Tong et al. (2010), and Lorito et al. (2011). The results from this study are listed as well.

## Figure Captions

**Figure 1:** Tectonic setting of the region surrounding the 2010 Mw 8.8 Maule earthquake, with the epicenter denoted by a red star. The approximate rupture extents of previous large earthquakes (yellow stars indicate the approximate epicenters) are shown shaded in pink. The green shaded region is the Constitución seismic gap. The subplots show the slip models by USGS (2010), Lay et al. (2010), Tong et al. (2010) and Lorito et al. (2011).

**Figure 2:** The useful sparsity that results from expanding localized geophysical signals in a Slepian basis. (a) Model-predicted coseismic gravity changes, as in Fig. 2a but now bandlimited to spherical harmonic degree and order 100; (b) an approximation of the same coseismic gravity changes using the  $N = 77$  best-localized of the 10201 Slepian functions concentrated to a circular region centered at the epicenter with radius of  $10^\circ$ ; (c) the differences between the spherical-harmonic representation in (a) and the Slepian-function representation in (b); (d) the corresponding 10201 spherical harmonic expansion coefficients; and (e) their Slepian expansion coefficients, using the same color scheme. Values whose absolute value is smaller than  $1/100$  of their maximum absolute value are rendered white. The ordinate is the sum of the rank  $\alpha$  of the Slepian function within a sequence of single absolute order and this order of  $|m|$ . Only a small number of Slepian functions are needed for an adequate representation of the signal in the target region.

**Figure 3:** Step functions fitted from time series of the Slepian coefficients when varying the center location of the concentration domain. (a) Amplitudes of the estimated step functions; (b) the Student  $t$ -values of the estimates. Solid dots indicate estimates that are significant at the 95% confidence level.

**Figure 4:** Time series of the Slepian expansion coefficients of the GRACE Level 2 Release 04 monthly gravity field solutions delivered by the Center for Space Research (CSR). Red: the original expansion coefficients. Blue: The residuals in the coefficients after removing the periodic variations fitted by the least-squares estimation. First column: the concentration region centered at the epicenter ( $72.9^\circ\text{W}$ ,  $35.8^\circ\text{S}$ ).

Second column: the concentration region centered east of the epicenter (at 69.9°W, 35.8°S).

**Figure 5:** The coseismic gravity changes, in units of  $\mu\text{Gal}$ , from the 2010 Mw 8.8 offshore Maule (Chile) earthquake obtained using spatio-spectral Slepian localization analysis of monthly GRACE solutions. The red star denotes the epicenter. The approximate rupture extents of previous large earthquakes (yellow stars indicating their approximate epicenters) that are located in the Andean subduction zone are shaded in pink. The green shaded area is the Constitución seismic gap. Grey lines indicate three profiles on which the GRACE observed gravity changes are used to invert for fault parameters.

**Figure 6:** (a) Model-predicted coseismic gravity changes, as in Fig. 2a but now bandlimited to spherical harmonic degree and order 60; (b) an approximation of the same coseismic gravity changes using only the 1<sup>st</sup> and 3<sup>rd</sup> Slepian functions concentrated to a circular region centered at the epicenter with radius of 10°; (c) the differences between the original model prediction in (a) and the partial Slepian-function representation in (b).

**Figure 7:** Coseismic gravity changes ( $\mu\text{Gal}$ ) predicted from the seismic fault models. (a) As inferred by adding the effect of the vertical motion of the surface shown in (b) to the effect due to internal density changes (compression and dilatation) shown in (c) from Model I; (d)–(f) are similar to (a)–(c) but predicted by Model II; (g)–(i) are similar to (a)–(c) but predicted by Model III; (j)–(l) are similar to (a)–(c) but predicted by Model IV. The data shown in each panel have been smoothed with an isotropic Gaussian filter having a radius of 350 km. The red star denotes the location of the epicenter, at 35.909°S and 72.733°W (U.S. Geological Survey, Magnitude 8.8 offshore Maule, Chile, 2010, <http://earthquake.usgs.gov/earthquakes/recenteqsww/Quakes/us2010tfan.php>).

**Figure 8:** Comparisons of coseismic gravity changes for the profiles along 32°S (left), 36°S (middle) and 39°S (right) between GRACE observations (shading indicates the estimated error) and the predictions from the four finite-fault models.

**Figure 9:** The coseismic gravity changes (at spatial resolution of 350 km) along an east-west profile across the middle of the fault plane for synthetic faulting scenarios: (Left) Fault length, depth, dip, strike, rake are fixed at 500 km, 4 km, 15°, 19°, and 90°, respectively. The width of the fault plane varies from 150 km to 250 km with steps of 50 km, and the uniform slip on the fault plane take values from 6 m to 10 m for each width. (Right) Fault-plane length, width, dip, strike and rake are fixed at 500 km, 150 km, 15°, 19°, and 90°, respectively. The depth of the top edge of the fault varies from 4 km to 6 km in steps of 1 km, and the uniform slip on the fault plane take values from 6 m to 9 m for each width. This example shows the sensitivity of coseismic gravity changes to faulting parameters.

**Figure 10:** The sensitivity of coseismic gravity changes (at spatial

resolution of 350km) to fault width and length in map view. The fault dip, strike and rake are fixed to be 16°, 17.5°, and 90°, respectively. The upper edge of the fault is fixed at 5 km depth, and the slip is fixed to be 7 m uniformly. Each row has the same fault-width value, which is 50 km, 150 km and 250 km for the 1<sup>st</sup>, 2<sup>nd</sup> and 3<sup>rd</sup> rows, respectively. Each column has the same fault-length value, which is 300 km, 600 km and 900 km for the 1<sup>st</sup>, 2<sup>nd</sup> and 3<sup>rd</sup> columns, respectively.

Figure 1

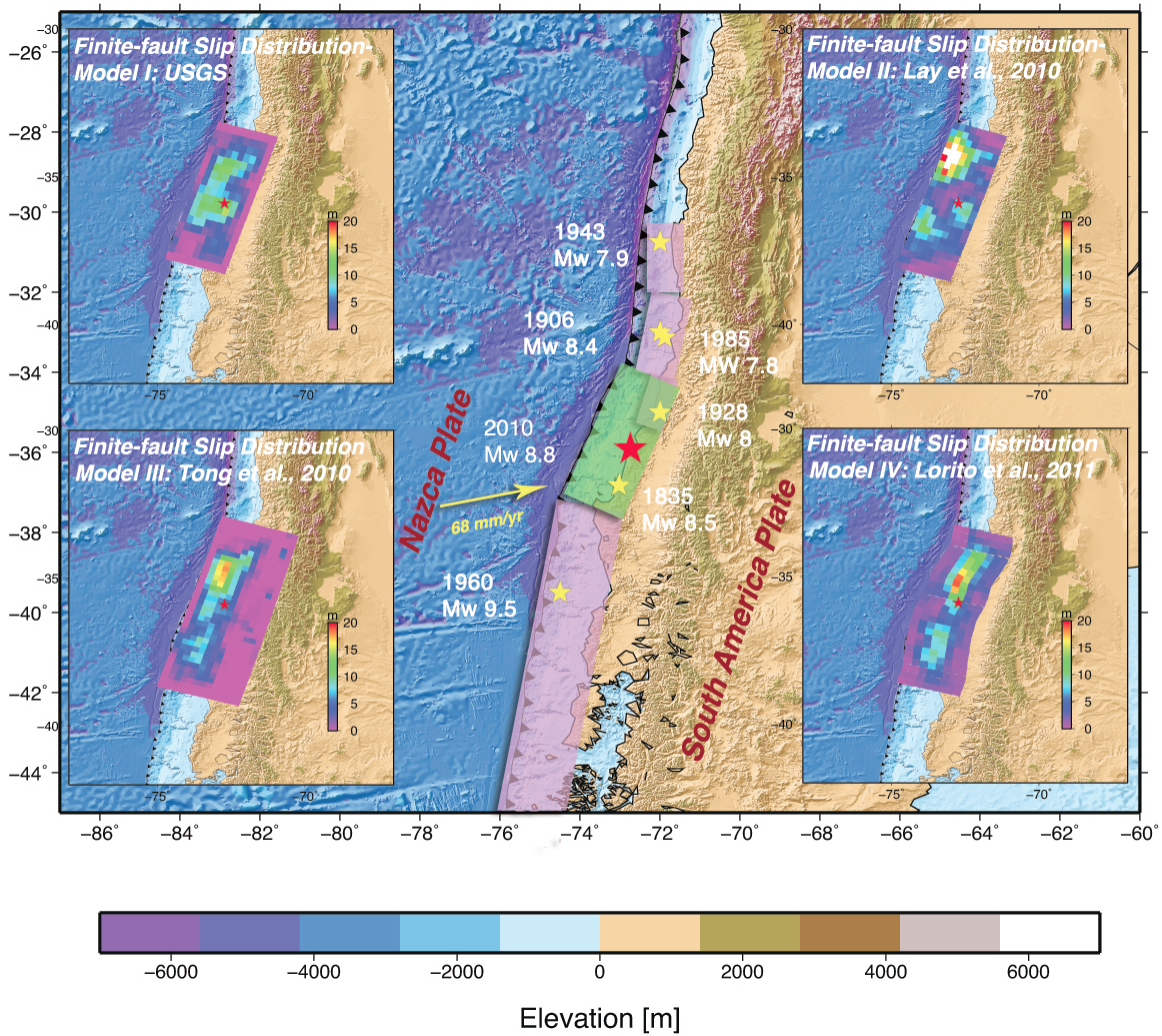


Figure 2

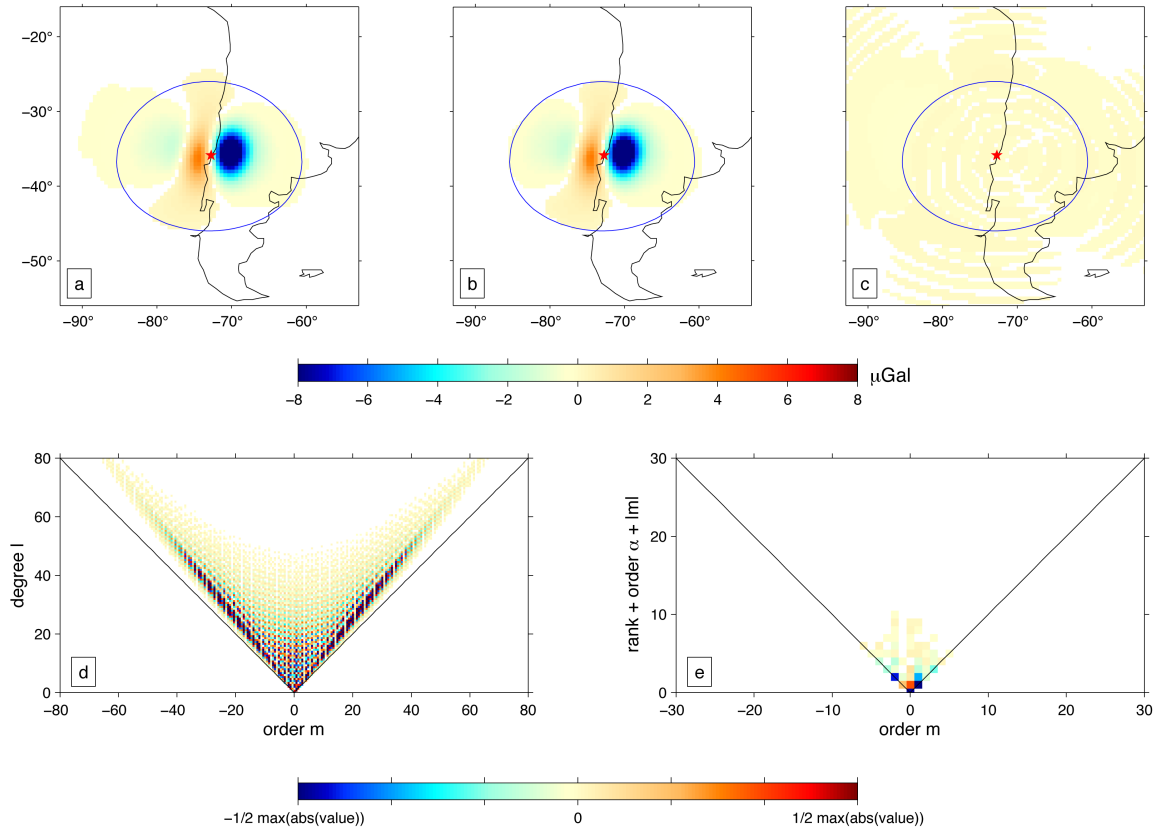


Figure 3

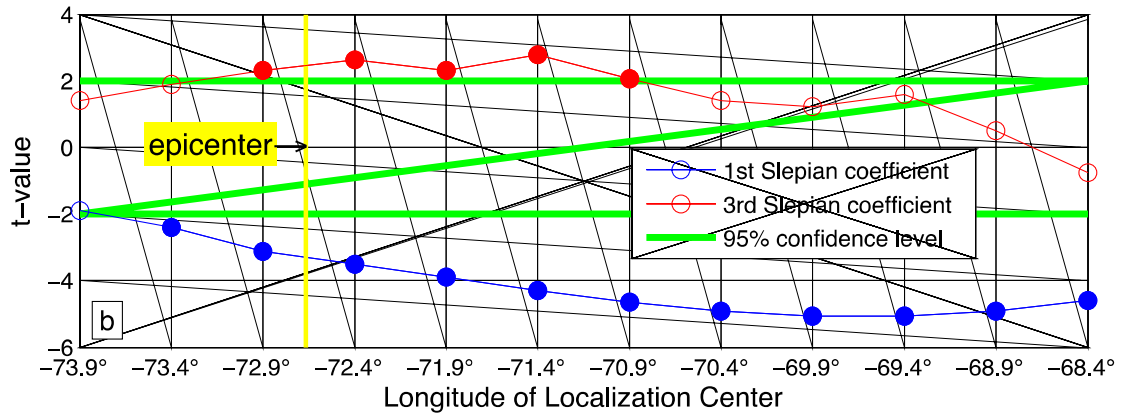
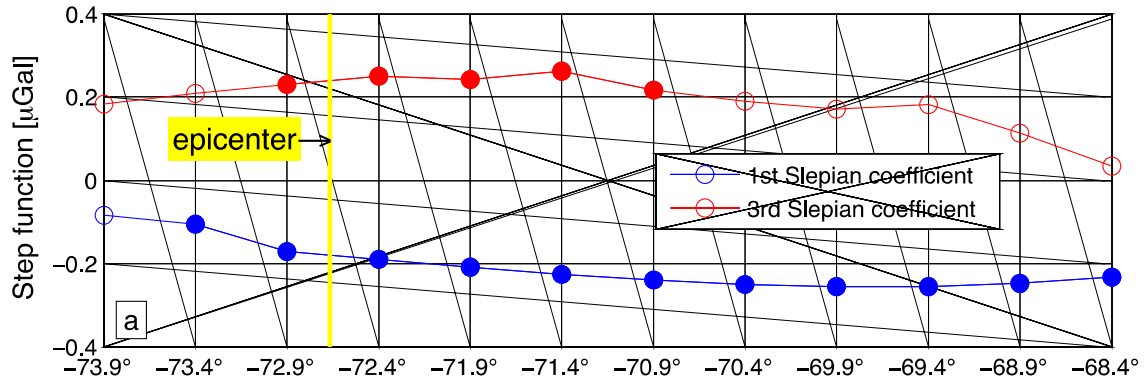


Figure 4

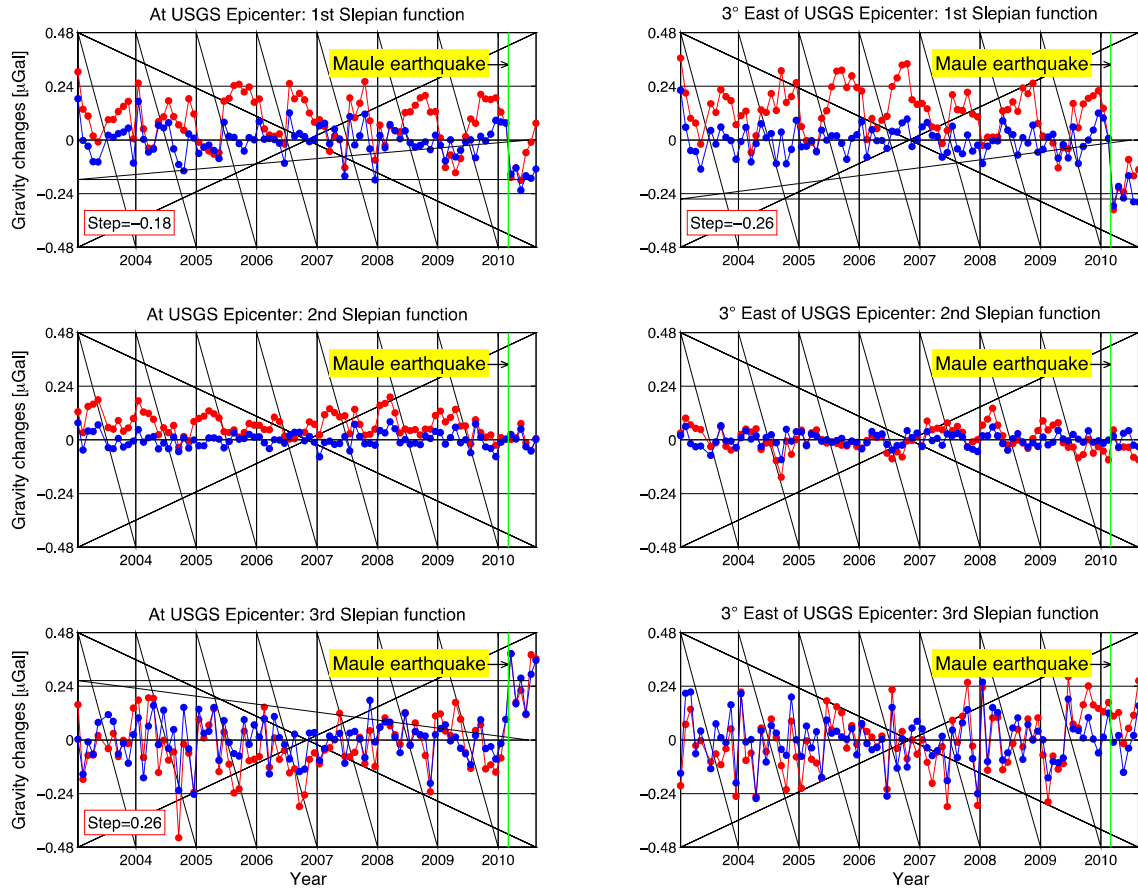


Figure 5

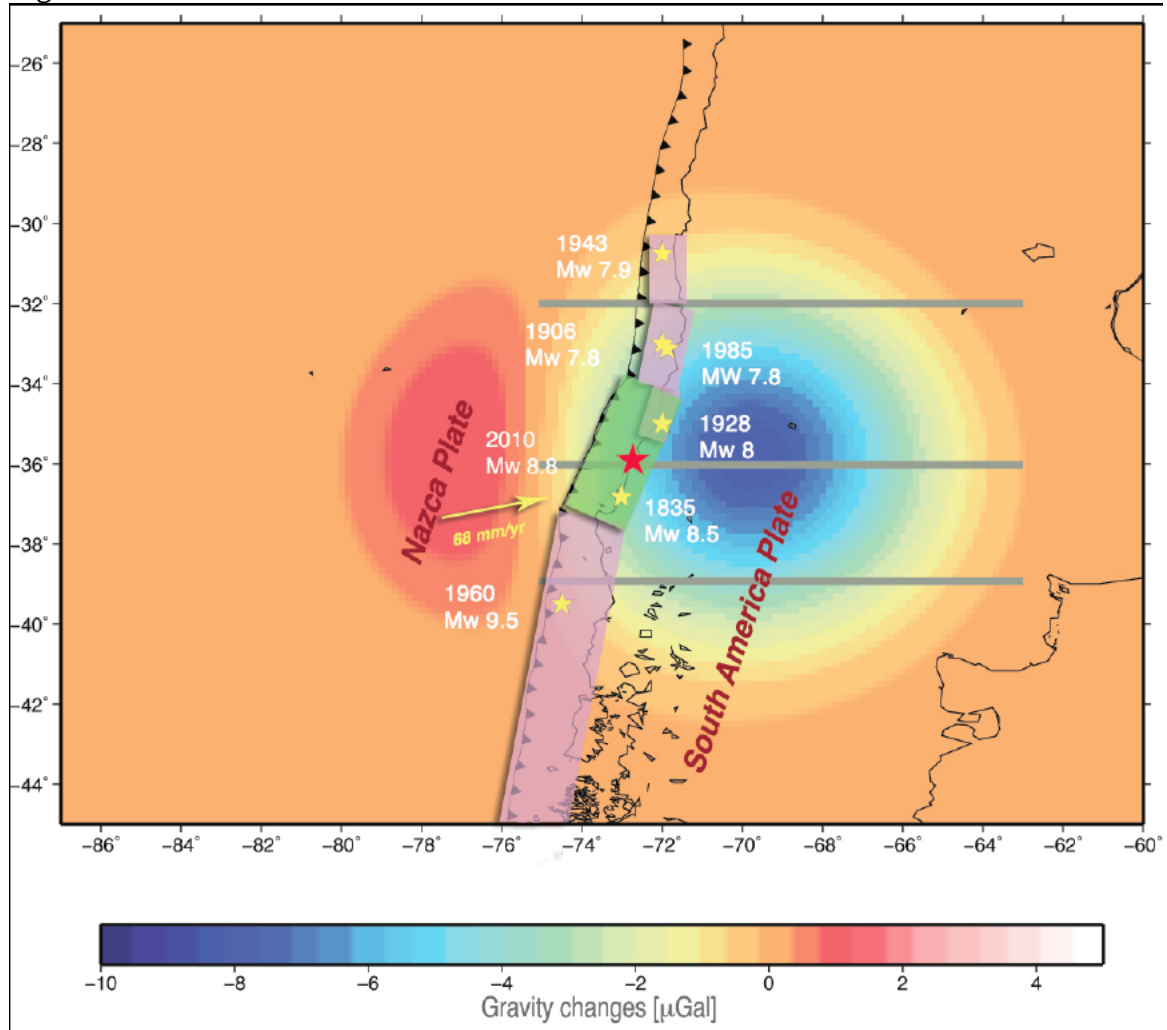


Figure 6

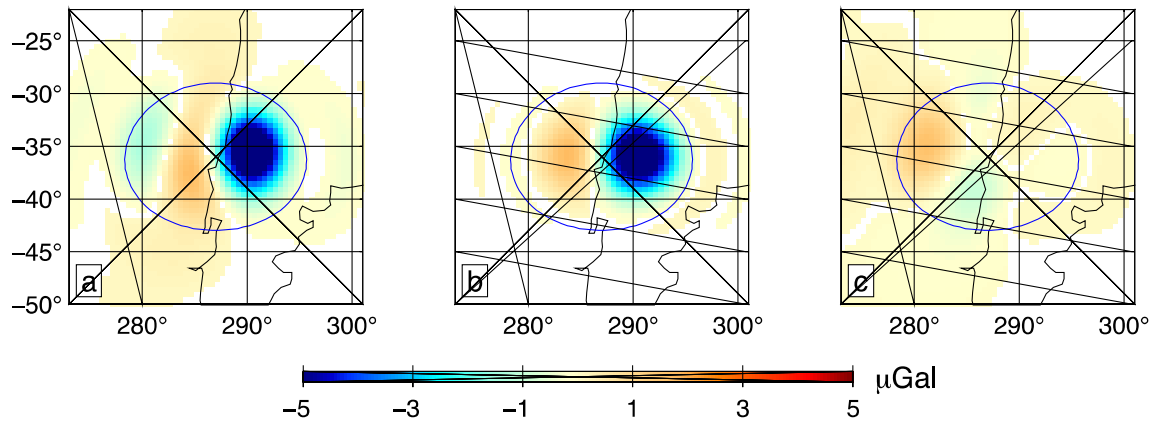


Figure 7

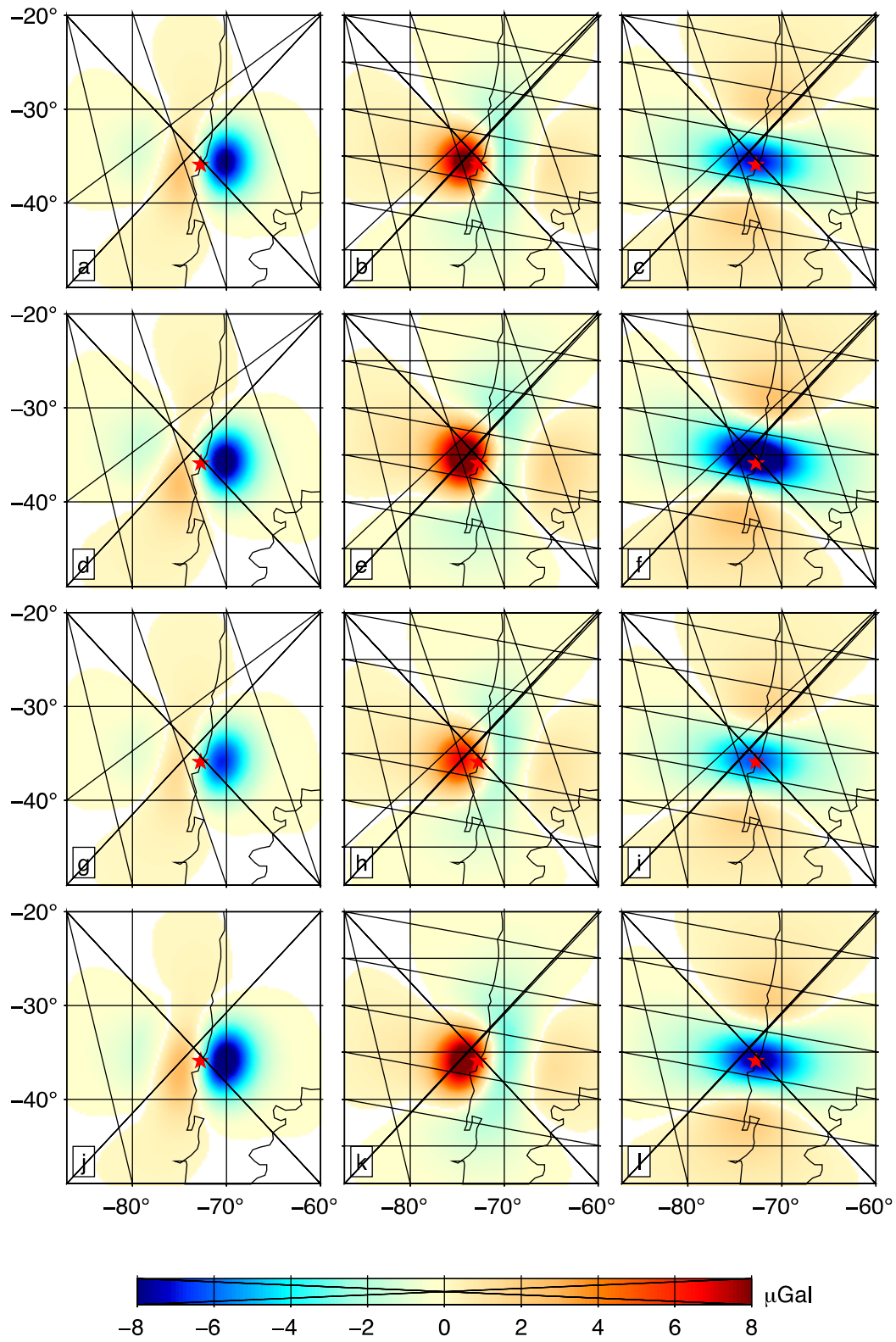


Figure 8

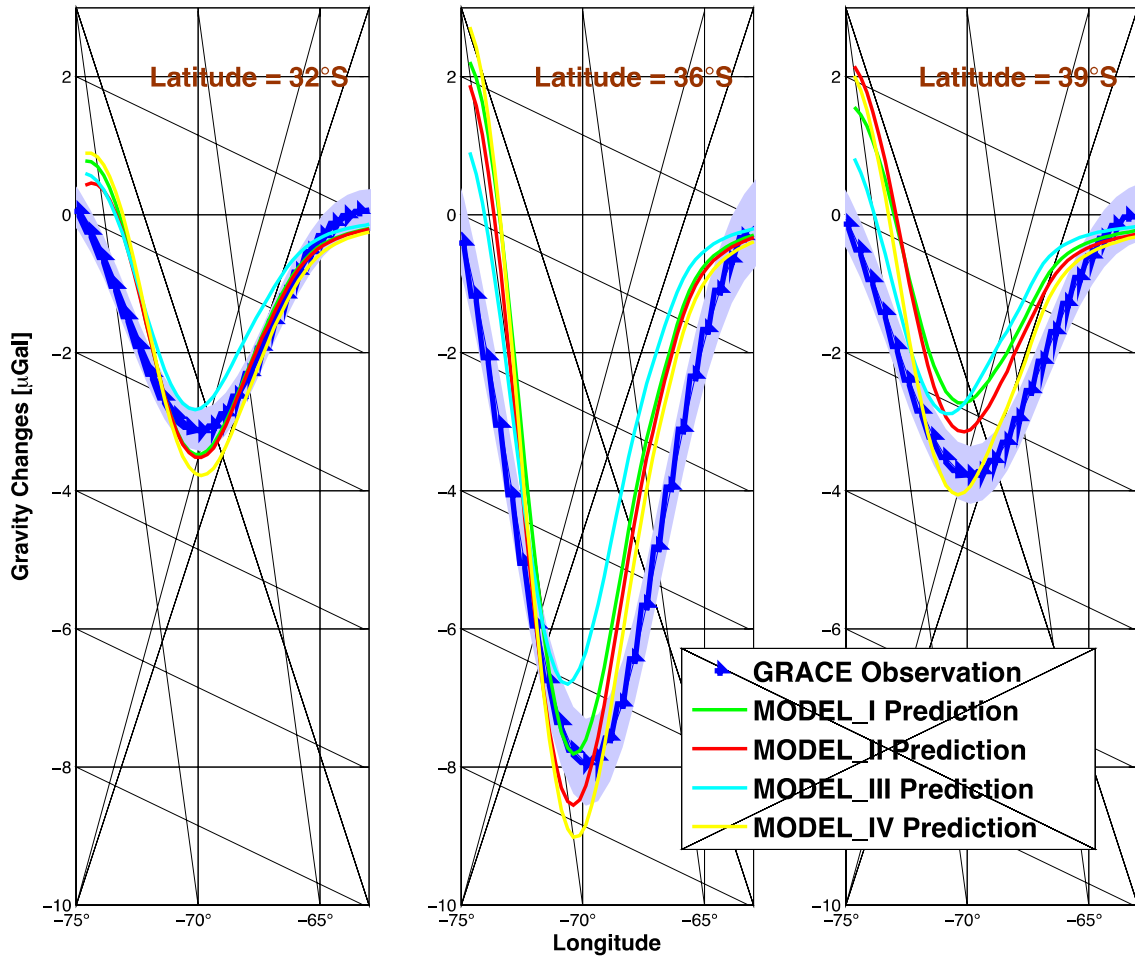


Figure 9

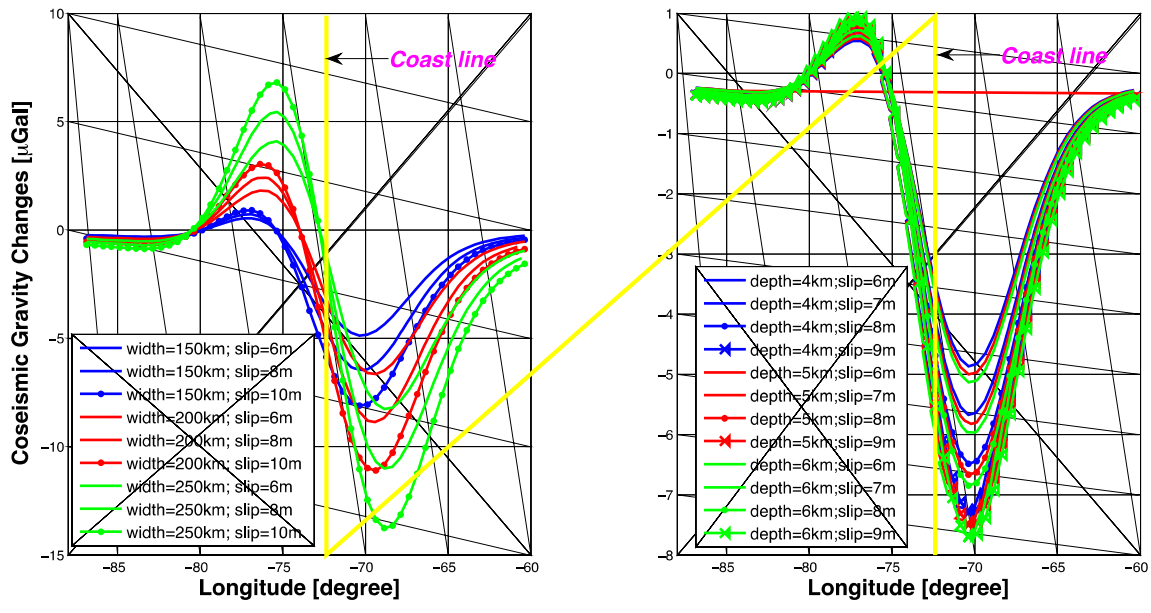


Figure 10

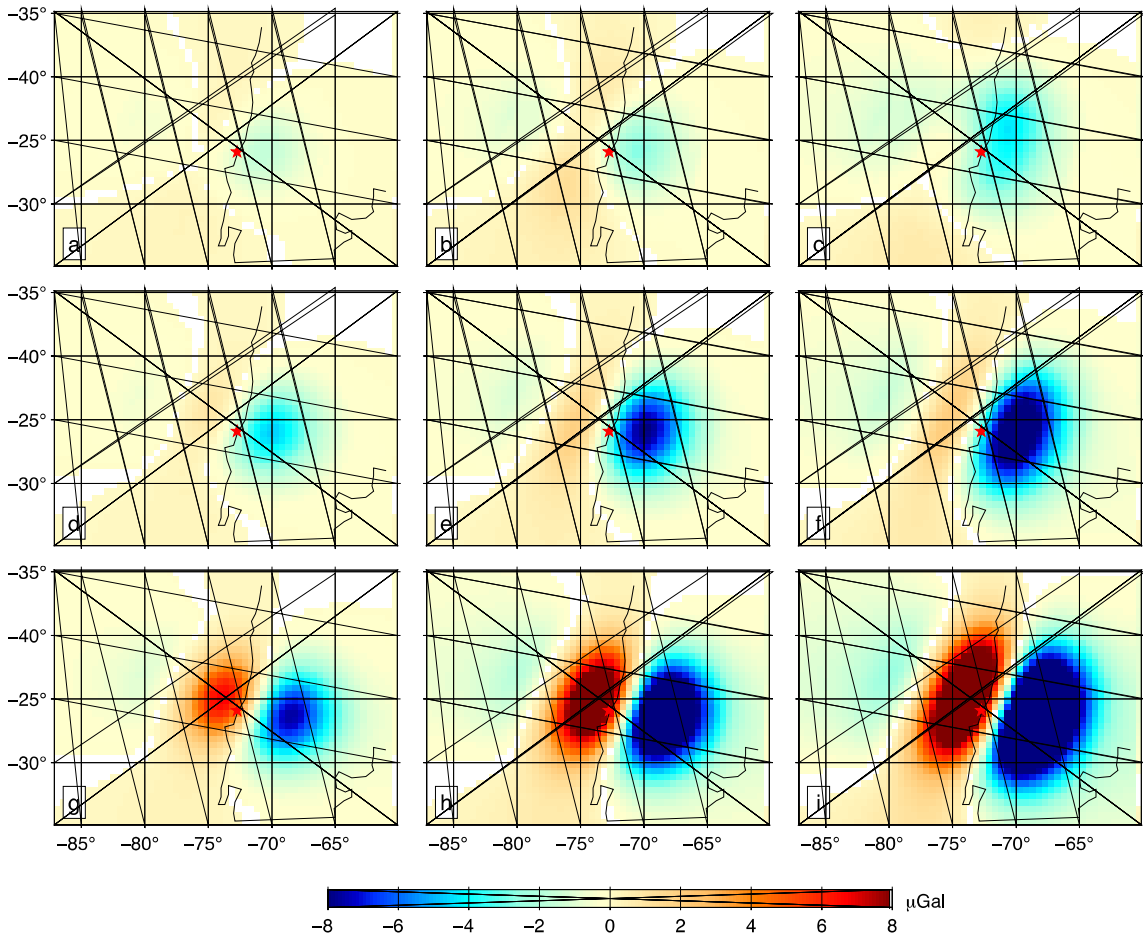


Table 1

|                   | <b>Fault plane</b> |              | <b>Top edge depth</b> | <b>Strike</b> | <b>Dip</b> | <b>Max slip</b> | <b>Depth of max slip</b> | <b>Potency [km<sup>2</sup>cm]</b> | <b>Data source</b>  |
|-------------------|--------------------|--------------|-----------------------|---------------|------------|-----------------|--------------------------|-----------------------------------|---------------------|
|                   | <b>Length</b>      | <b>Width</b> |                       |               |            |                 |                          |                                   |                     |
| <b>Model I</b>    | 540 km             | 200 km       | 2.9 km                | 17.5°         | 18°        | 14.6 m          | 39.9 km                  | 4.6x10 <sup>7</sup>               | Teleseismic waves   |
| <b>Model II</b>   | 575 km             | 180 km       | 4 km                  | 18°           | 18°        | 27.8 m          | 10.3 km                  | 6.3x10 <sup>7</sup>               | Teleseismic waves   |
| <b>Model III</b>  | 669.8 km           | 260 km       | 2.6 km                | 16.8°         | 15°        | 18.0 m          | 18.1 km                  | 5.7x10 <sup>7</sup>               | InSAR, GPS          |
| <b>Model IV</b>   | ~625 km            | ~200 km      | 9 km                  | 2°–30°        | 10°~22°    | 18.8 m          | 28.0 km                  | 5.5x10 <sup>7</sup>               | InSAR, GPS, tsunami |
| <b>This study</b> | 429 km             | 146 km       | 5 km                  | 19°           | 15°        | 8.1 m (uniform) | –                        | 5.1x10 <sup>7</sup>               | GRACE               |